Available online at www.sciencedirect.com

ScienceDirect

Journal of Magnesium and Alloys 12 (2024) 1346–1366

www.elsevier.com/locate/jma

Full Length Article

Interplay of laser power and pore characteristics in selective laser melting of ZK60 magnesium alloys: A study based on *in-situ* monitoring and image analysis

Weijie Xie[a,b], Hau-Chung Man[a,c,*], Chi-Wai Chan[b,*]

[a] *Department of Industrial and Systems Engineering, The Hong Kong Polytechnic University, Hong Kong, China*
[b] *School of Mechanical and Aerospace Engineering, Queen's University, Belfast BT9 5AH, UK*
[c] *Research Institute for Advanced Manufacturing, The Hong Kong Polytechnic University, Hong Kong, China*

Received 26 July 2023; received in revised form 5 October 2023; accepted 2 November 2023
Available online 10 December 2023

Abstract

This study offers significant insights into the multi-physics phenomena of the SLM process and the subsequent porosity characteristics of ZK60 Magnesium (Mg) alloys. High-speed in-situ monitoring was employed to visualise process signals in real-time, elucidating the dynamics of melt pools and vapour plumes under varying laser power conditions specifically between 40 W and 60 W. Detailed morphological analysis was performed using Scanning-Electron Microscopy (SEM), demonstrating a critical correlation between laser power and pore formation. Lower laser power led to increased pore coverage, whereas a denser structure was observed at higher laser power. This laser power influence on porosity was further confirmed via Optical Microscopy (OM) conducted on both top and cross-sectional surfaces of the samples. An increase in laser power resulted in a decrease in pore coverage and pore size, potentially leading to a denser printed part of Mg alloy. X-ray Computed Tomography (XCT) augmented these findings by providing a 3D volumetric representation of the sample internal structure, revealing an inverse relationship between laser power and overall pore volume. Lower laser power appeared to favour the formation of interconnected pores, while a reduction in interconnected pores and an increase in isolated pores were observed at higher power. The interplay between melt pool size, vapour plume effects, and laser power was found to significantly influence the resulting porosity, indicating a need for effective management of these factors to optimise the SLM process of Mg alloys.

Keywords: Selective laser melting (SLM); Magnesium (Mg) alloys; Biodegradable implants; Porosity; In-situ monitoring.

1. Introduction

Magnesium (Mg) alloys have emerged as a promising alternative to conventional biomedical implant materials such as titanium (Ti) and stainless steels. Their unique biodegradability and biological compatibility make them well-suited for use in cardiovascular stents and temporary fixation devices (e.g., fracture fixation screws and pins) [1]. This biodegradability eliminates the need for a second surgery to remove the implants as they degrade harmlessly in the body, reducing long-term complications. The applications of Mg alloys extend beyond the biomedical field, contributing to enhanced fuel efficiency in the automotive industry and structural integrity in the aerospace and space industries due to their lightweight properties and high strength-to-weight ratio [2]. Yet, regardless of their diverse applications, the critical challenge of managing their degradation rate remains, emphasising the need for focused investigations. This concern, primarily impacted by material porosity [1,3], is prevalent not only in the biomedical field but also in the aforementioned sectors, where material durability and integrity are the key issues.

Manufacture of Mg parts by conventional methods (e.g., forming, casting, machining, etc.) presents significant chal-

* Corresponding authors.
E-mail addresses: hc.man@polyu.edu.hk (H.-C. Man), c.w.chan@qub.ac.uk (C.-W. Chan).

https://doi.org/10.1016/j.jma.2023.11.005

lenges. These methods always involve multiple processes to control microstructure and shape complex geometries [2]. Furthermore, porosity, as an influential factor in Mg degradation, is hard to regulate. These limitations have led to the rise in popularity of Selective Laser Melting (SLM). SLM is an advanced metal 3D printing process. It enables the direct manufacture of Mg alloys with intricate designs and improved microstructural properties in a single step [4,5]. However, SLM is also a complex process, involving numerous interrelated parameters, such as laser power, scanning speed, layer thickness, etc. Each of these plays a unique role. For instance, the laser power has a direct effect on the melting process, while the scanning speed and layer thickness are primarily responsible for determining the cooling rate and the degree of overlap between layers, respectively. The delicate balance and interplay among these parameters can significantly impact the degree of porosity in Mg alloys [4,6]. A study by Deng et al. [7] highlighted the significance of laser power over scanning speed in affecting the porosity during the SLM process. When the Mg alloys are fabricated using optimised SLM parameters, densities up to 93% can be achieved [8]. In some cases, full density can be obtained [2]. Besides, the use of in-situ process monitoring via a high-speed camera provides real-time observations of the SLM process, generating valuable data on how process signals, such as melt pool dynamics and vapour plume, dynamically change under different parameter settings [9,10]. This can lead to a more in-depth understanding of how process parameters impact the porosity of printed parts.

Porosity is a common occurrence in SLM-printed parts, including Mg alloys. It refers to the presence of voids (or pores) within the printed materials. Porosity can significantly influence the degradation properties of Mg alloys, accelerating their degradation [3]. Therefore, understanding the characteristics of porosity, including size, type, and distribution, is fundamental to controlling these degradation properties and extending the lifespan of implants. While there is a significant body of research investigating the effect of porosity on the properties of SLM-printed parts, the focus has largely been on Ti-6Al-4V and stainless steels [11–16]. Gong et al. [11]. observed that minor pores (<50 μm), constituting up to 1% of the total volume in Ti-6Al-4V, had negligible impact on tensile strength. Biswal et al. [12] found that the internal pore shape and position can influence the fatigue strength of SLM-processed Ti-6Al-4V, potentially more than the pore size itself. Stef et al. [13] indicated that the existence and 3D arrangement of porosity affect both tensile toughness and crack path in Ti-6Al-4V. Regarding stainless steels, Suryawanshi et al. [14] pointed out that aggressive ions (i.e., chloride ions) tend to gather in surface pores, thereby accelerating the corrosion process. In line with this, Wang et al. [15] reported that the level of porosity and corrosion resistance in SLM-printed stainless steels are inversely related, with enclosed sub-surface pores displaying vulnerability to pitting corrosion. Yang et al. [16] similarly revealed that increased porosity levels make SLM-printed stainless steels more likely to suffer pitting corrosion, leading to formation of unstable passive films that are easily compromised.

From the literature, it is evident that porosity has a significant impact on both mechanical and corrosion properties of materials. Previous studies on Ti-6Al-4V and stainless steels illustrate that the effects of porosity can range from negligible to highly significant depending on pore size, shape, and location. Whilst the current study primarily focuses on the analysis of pore characteristics in SLM-printed Mg alloys, it is important to recognise that the broader implications of porosity on their degradation properties remain underexplored. In biomedical applications, where the degradation behaviour of SLM-printed Mg alloys is vital, a thorough understanding of porosity becomes crucial.

Two primary methods are generally employed to understand and measure porosity in the SLM-printed alloys: non-destructive and destructive techniques. In terms of non-destructive methods, X-ray computed tomography (XCT) is widely used. It allows a quick and comprehensive 3D porosity analysis without damaging the sample. While XCT has gained significant attention in the literature for analysing porosity in SLM-printed parts, most of these studies have focused on Ti-6Al-4V [17–20] and stainless steels [21–24]. Notably, none have specifically investigated the porosity of SLM-printed Mg alloys using this technique.

Despite their intrusive nature, destructive methods (i.e., optical microscopy, OM and scanning electron microscopy, SEM), provide more detailed insights into porosity characteristics [25]. They facilitate a high-resolution examination of size, type, and distribution of isolated pores. In comparison, XCT often faces challenges in detecting and analysing pores below its resolution limit. It is important to note that neither XCT, OM, nor SEM can independently provide a holistic understanding of porosity. Thus, a combined approach utilising both non-destructive and destructive methods is essential. It ensures a comprehensive understanding of porosity in SLM-printed Mg alloys.

The current study aims to address the gaps in our understanding of porosity in the SLM-printed Mg alloys, posing several key research questions. First, how does different energy input, achieved through the modulation of laser power, influence the characteristics of porosity? Second, how can in-situ monitoring of the SLM process aid in correlating process signals with porosity? Third, is it possible to establish classification rules for different porosity characteristics, such as size and type, to facilitate detailed porosity analysis? Lastly, can a combined analysis employing XCT (non-destructive), as well as OM and SEM (destructive methods), yield a comprehensive understanding of porosity?

By answering these questions, this study seeks to significantly advance the understanding of porosity control for SLM-printed Mg alloys. The novelty of this research lies in its holistic approach, which integrates in-situ monitoring, variation in laser power, and a combined application of non-destructive (XCT) and destructive (OM and SEM) porosity analysis methods.

Table 1
Elemental composition of ZK60 Mg powders for SLM experiments in this study.

Composition	Mg	Zr	Zn	Fe	Mn	Ni	Si	Cu	Al
wt.%	94.46	0.33	5.1953	0.0035	0.0055	0.003	0.0007	0.001	0.0006

2. Materials, experiments and methodology

2.1. Materials, SLM process and in-situ monitoring by high-speed camera

Spherical ZK60 Mg powders, which were sourced from TangShan WeiHao Ltd., China, were utilised in this study. Their particle size varied from 20 to 63 μm, with a d_{50} measurement of 38 μm. The elemental composition of these powders is shown in Table 1. Prior to the SLM process, the powders underwent drying in a vacuum at 60 °C for 48 hours, achieving a humidity level of 5%. ZK60 was chosen because of its commercial availability, non-toxicity, and significant potential in biomedical applications [4].

The study employed a Selective Laser Melting system, SLM®125 (SLM Solutions Group AG, Germany), equipped with a continuous-wave Yb-doped Fibre laser (wavelength 1070 nm), for the manufacturing process. The process was carried out in a chamber that was saturated with ultra-high purity argon gas (99.999%). Given the high reactivity of Mg powders with oxygen, the oxygen levels within the chamber were maintained below 100 ppm throughout the SLM process. The pressure inside the chamber was set to 50 mbar.

In the context of SLM, a substrate plate made of stainless steel was used due to its high melting point, good thermal conductivity, and low thermal expansion coefficient. These properties make it an ideal base for the SLM process, providing stability and support during the formation of the samples. The substrate plate was pre-heated to 100 °C to mitigate thermal stress by minimising the thermal gradient in the melt pool.

The scanning strategy adopted for this study is illustrated in Fig. 1(a). During the initial stage of the SLM process, it is important to ensure strong adhesion between the fabricated parts and the substrate plate. To meet this requirement, the first layer printing was repeated four times, securing a robust bond for the layers that followed. The cylindrical ZK60 Mg samples, displayed in Fig. 1(b), with a diameter of 6 mm and a thickness of 3 mm, were produced at three different laser powers: 40 W, 50 W, and 60 W. Each sample was built from a total of 100 layers, and each set of conditions was repeated 45 times, resulting in a total of 135 samples. These were then used for a variety of characterisations and analyses. The laser scanning speed, laser spot size, and layer thickness remained constant across all samples, set at 600 mm/s, 123.4 μm, and 30 μm, respectively.

After the SLM process, the samples were separated from the stainless-steel substrate using wire-cutting techniques to ensure a precise and smooth cut without damaging the samples.

In-situ monitoring during the SLM process has become an area of considerable interest for both industry and academia, driven by the relatively high failure rate of SLM products and the substantial costs associated with the process. To further investigate the complexities of the SLM process, this study utilised a high-speed camera (NPX-GS6500UM, GongYeShi-Jie Ltd., China) capable of recording at 460 fps. The high-speed camera facilitated real-time observations of transient phenomena in the SLM process such as melt pool dynamics and vapour plume behaviour.

To compare the size of the melt pool under different laser powers (40 W, 50 W, and 60 W), screenshots of process signals, spanning time frames from 0 s up to 500 ms in 50 ms intervals, were converted into 8-bit images. These images were subsequently analysed using the ImageJ software. Within an 8-bit image, the grey value, which is influenced by the amount of light a pixel absorbs, can range from 0 to 255. A pixel presenting a higher grey value is brighter, while a lower value indicates a darker pixel. Pixels possessing a grey value of 255, which appear white, provide a metric for determining the size of the melt pool. This is due to the radiant intensity and inherent brightness associated with the melt pool. These attributes can be effectively captured using the image processing technique as described by Berumen et al. [26].

2.2. Sample polishing

Following the SLM manufacturing process, the samples were cleansed with 99.5% ethyl alcohol (Thermo Fisher Scientific Inc., USA) in an ultrasonic bath for 10 minutes. They were then thoroughly dried in a dry box, maintaining a humidity level of less than 30%.

Afterwards, the samples were hot mounted and polished in preparation for further examination. An automatic polishing machine (AutoMet 250, Buehler Ltd., USA) was employed for this purpose. It is important to note that magnesium alloys, such as the ZK60 Mg in this study, are generally regarded as challenging to polish due to their high reactivity and relatively low hardness.

The polishing protocol encompassed several steps. The initial step involved the use of a P400 SiC paper under a load of 20 N and a speed of 200 rpm until the surface was planar. Subsequent stages employed oil-based diamond slurries of different granularities: a 9-μm slurry applied for 6 minutes at 150 rpm, a 3-μm slurry used for 5 minutes at 100 rpm, and finally, a 1-μm slurry for 4 minutes, again at 100 rpm.

To minimise exposure to air, the ZK60 Mg samples were quickly rinsed with distilled water and immediately immersed in 99.5% ethanol (Thermo Fisher Scientific Inc., USA) after

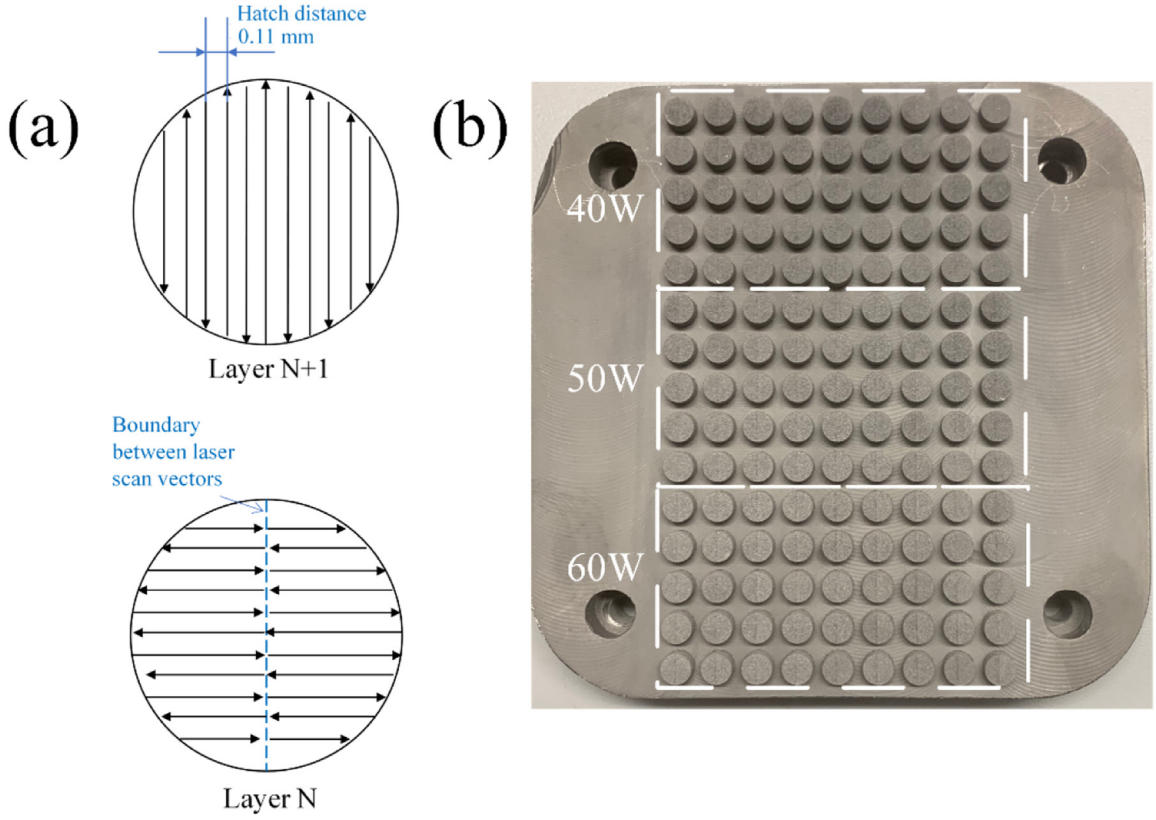

Fig. 1. (a) Laser scanning strategy adopted in the SLM process of ZK60 Mg samples. The black arrows indicate the laser scan vectors; (b) the SLM-printed cylindrical Mg samples by different laser powers between 40 W and 60 W. Each set of laser conditions was repeated 45 times.

each polishing stage. They were then ultrasonically cleaned for approximately 5 minutes. Following the polishing, the samples were promptly placed in a vacuum desiccator with a pressure of around 0.14 bar and left undisturbed for at least 24 hours prior to further inspection.

2.3. Porosity analysis by OM

The porosity analysis conducted on the ZK60 Mg samples was carried out using an OM which comprises two components: a monocular microscope (AmScope H800-3PL, United Scope Europe BV, Netherlands), and a digital camera (AmScope MU2003, United Scope Europe BV, Netherlands).

A schematic illustrating the process of obtaining individual surface images and their subsequent combination to form the merged images of the entire surfaces can be seen in Fig. 2. Individual optical images were captured at 50x magnification for both the top and cross-sectional surfaces of the samples. Each individual optical image had a resolution of 5440 × 3648 pixels. Following this, multiple individual optical images from both surface types were combined to create merged optical images, which provide a comprehensive view of each surface type. To represent the entire top surface, approximately 30 individual images were used, while the entire cross-sectional surface was illustrated with around 15 images. The merged optical images were created using the EdrawMax software. The merged image, representing the entire top surface, had a resolution of 14,967 × 14,680 pixels, while the merged image of the entire cross-sectional surface had a resolution of 16,393 × 10,000 pixels.

Afterwards, these merged images were analysed using ImageJ software. As demonstrated in Fig. 3(a), black areas in optical images represent the pores on the samples. To isolate the effect of the background, its colour was altered to white using Adobe Photoshop. The Otsu thresholding algorithm was then implemented to derive the corresponding binary images, as shown in Fig. 3(b) [27]. This allowed for the determination of pore coverage and distribution on each sample. The Otsu algorithm is renowned for its ability to convert grayscale images into binary format by finding the threshold that minimises the intra-class variance of the grayscale levels. In the OM analysis, the pore coverage refers to the percentage of surface area occupied by the pores.

These binary images underwent further evaluation through the "particle analysis'' function in ImageJ. In this stage, as illustrated in Fig. 3(c), the size and morphology of each pore were quantitatively measured. The Feret Diameter was adopted to characterise pore size while circularity was used to characterise pore morphology.

In the fields of image analysis and microscopy, the Feret diameter serves as a tool to measure the size of an object in a designated direction within an image. It is defined by the distance between two parallel lines tangent to the boundary of the object. Two primary types of Feret diameters exist:

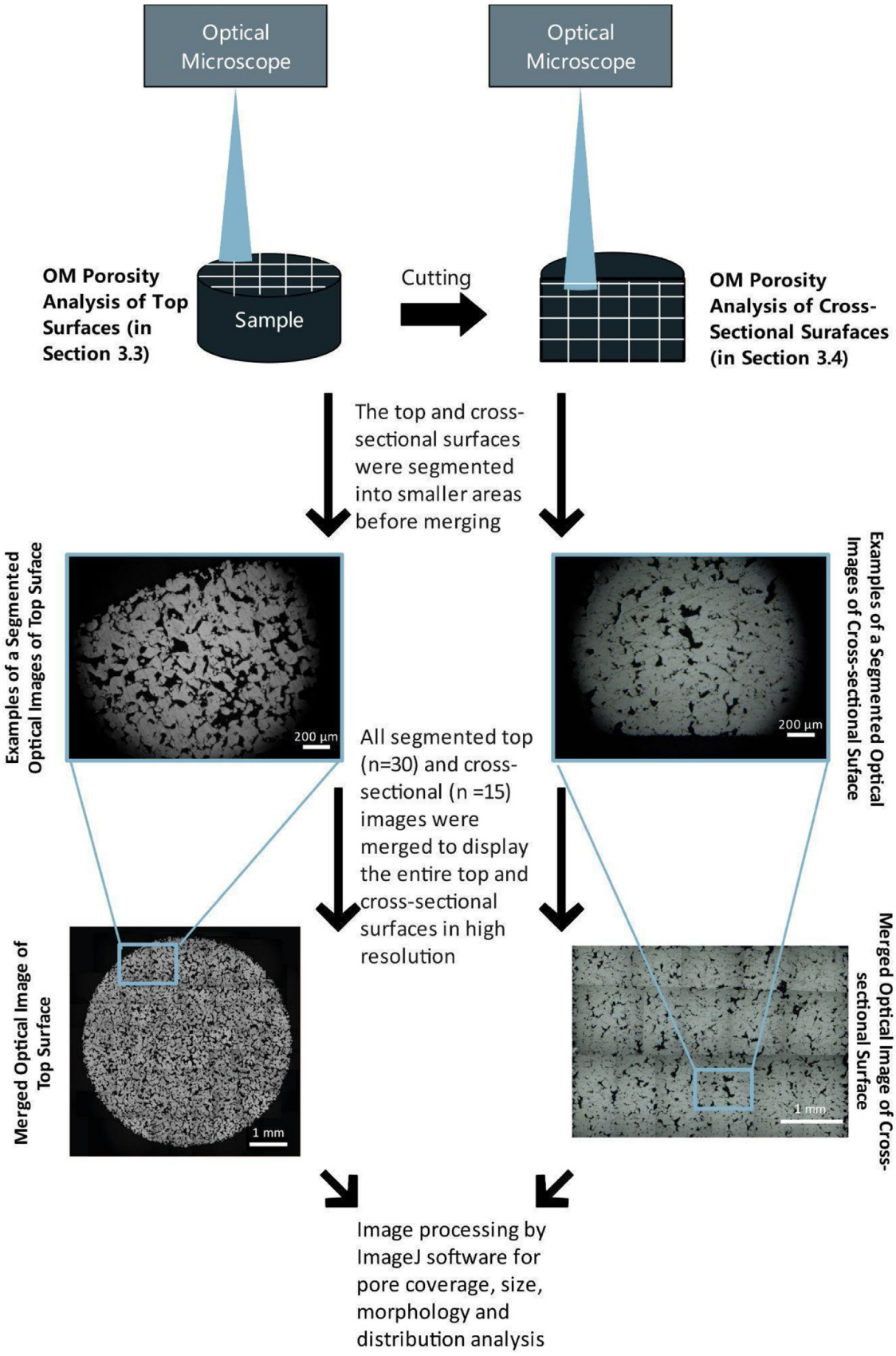

Fig. 2. A schematic diagram showing the methodology of obtaining and merging the optical images that represent the entire top and cross-sectional surfaces in the OM porosity analysis.

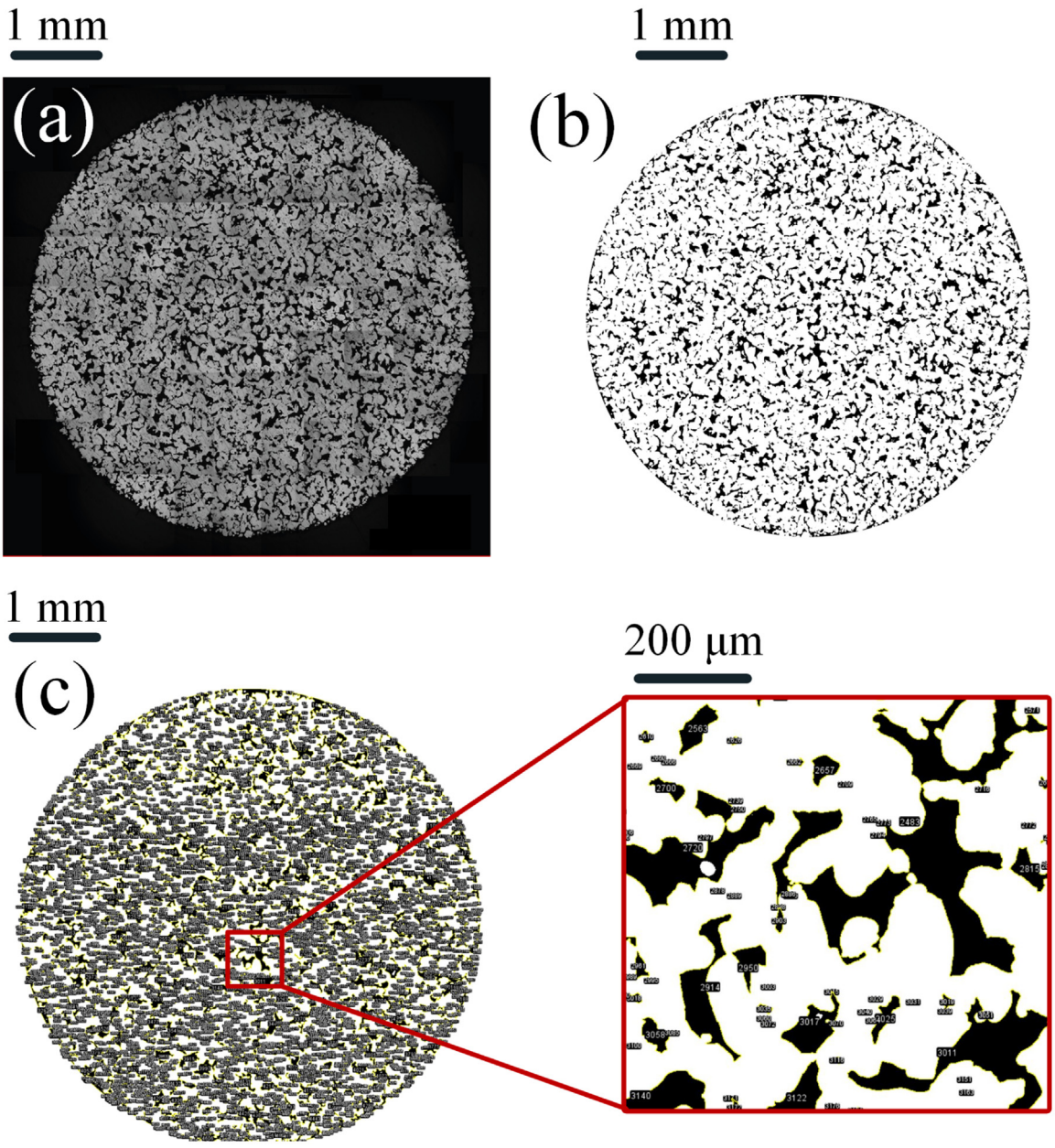

Fig. 3. Image processing procedures for porosity analysis; (a) the merged optical image; (b) the corresponding binary image obtained by Otsu thresholding algorithm; (c) particle analysis image by ImageJ with magnified view.

(i) the Maximal Feret Diameter, which represents the longest distance between any two points on the perimeter of the object, and (ii) the Minimal Feret Diameter, which indicates the shortest distance between parallel tangents touching the object from opposing sides. In this study, Maximal Feret Diameter was adopted. These measurements provide insights into the dimensions and morphology of the object. For a detailed understanding of the Feret Diameter and its computation methodology, one may refer to the study by Yap [28].

2.4. Error validation and surface morphology by SEM

To assess the accuracy of the OM method, nine pores were selectively imaged at random sample locations using both OM and SEM. Their areas were then measured, analysed and compared using ImageJ software. For the image extraction process, Adobe Photoshop was employed. With tools such as the Lasso, pores were manually isolated from the images. These pores were subsequently saved as individual files on separate layers for further analysis. The imaging instruments used were the Zeiss Axiolab 5 optical microscope (Germany) for OM and the Tescan VEGA3 SEM (Czech) for SEM.

Additionally, the surface morphology of ZK60 Mg samples, produced at 40 W, 50 W, and 60 W, was examined using SEM at magnifications of x400, x1k, and x3k. Surface contaminants were eliminated through polishing before observation.

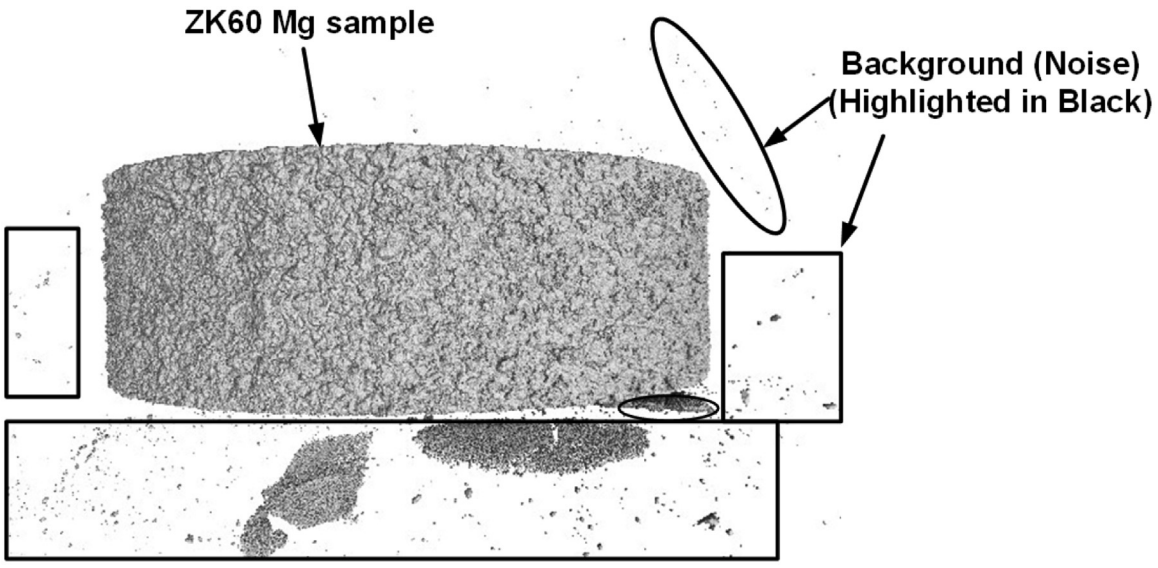

Fig. 4. Example of Mg sample reconstructed in XCT analysis with a CNR value of 1. The background noise is highlighted in black, requiring to be filtered manually.

2.5. Porosity analysis by XCT

In addition to the OM analysis for porosity, XCT was also employed to measure and analyse the porosity of different samples. The model of XCT machine was YXLON FF20 CT (YXLON International GmbH, Germany), equipped with VGStudio Max 3.0 software. During the measurement, the tube generated a Femtosecond X-ray Experiment (FXE) transmission beam, operating at 90 kV voltage and 70 μA current. While higher voltage and current can produce more high-energy X-rays, they also increase the number of lower-energy X-rays prone to scattering, which intensifies noise [29]. To mitigate this noise, a 1 mm thick aluminium filter was employed and the machine utilised 1080 projections.

The voxel size is closely related to the sample size. For the cylindrical ZK60 Mg samples measured in this study, as shown in Fig. 1(b), the voxel size was 3.8 μm. The XCT porosity analysis was conducted using the VGStudio Max 3.0 software. It is noteworthy that the minimum volume of 8 voxels, which corresponds to a 2 × 2 × 2 matrix, acts as a baseline filter to screen out potential noise or insignificant micro-pores that might not have a substantial impact on the pore coverage and distribution analysis. This focuses the analysis on pores of relevant size that can affect material properties. On the other hand, the threshold of 125 voxels, represented by a 5 × 5 × 5 matrix, is typically used to gain insights into pore morphology. This higher threshold ensures that only the more significant, well-defined pores are analysed, providing a clearer picture of the pore structure and interconnectivity without being skewed by smaller, potentially irregular pores. It is important to note that the selected voxel thresholds align with the practices and resolution constraints from the literature [25,30,31]. Adhering to these guidelines mitigates inaccuracies and ensures the results are valid and comparable with other studies in the field. Presuming that the pores are spherical in shape, the equivalent diameter of 8 voxels was 9.3 μm, while that of 125 voxels was 23.3 μm. It is noted that in XCT analysis, pore coverage denotes the volume fraction of porosity. Given that pores are viewed as a distinct phase, their area fraction in the 2D slices is indicative of the volume fraction in the 3D structure [32].

The signal to noise ratio (SNR) and contrast to noise ratio (CNR) are employed to evaluate the image quality of representative reconstructed images in XCT [33]. They can be calculated using the following equations:

$$SNR = \frac{g_{material}}{\sigma_{material}}$$

$$CNR = \frac{g_{material} - g_{background}}{\sigma_{material}}$$

In both equations, $g_{material}$ and $g_{background}$ represent the average grey value for two selected regions of interest (ROIs), one inside the material and the other outside. σ_{object} and $\sigma_{background}$ represent the standard deviations for these respective ROIs.

In this study, the values determined for SNR and CNR were 23 and 1, respectively. While the SNR value indicated good image quality [34], the comparatively low CNR value implied challenges in differentiating the ZK60 Mg samples from their background [34], as further highlighted in Fig. 4. Consequently, manual removal of background noise was required. Traditional algorithms for porosity analysis in VGStudio Max, like the Only Threshold and Default algorithm, were found to be unsuitable for this study. Therefore, the Custom Defect Mask algorithm was employed. In this approach, the algorithm initially assigns a "probability'' value to potential defects (those larger than the resolution threshold). Only those with a probability value greater than 1 are identified as porosities.

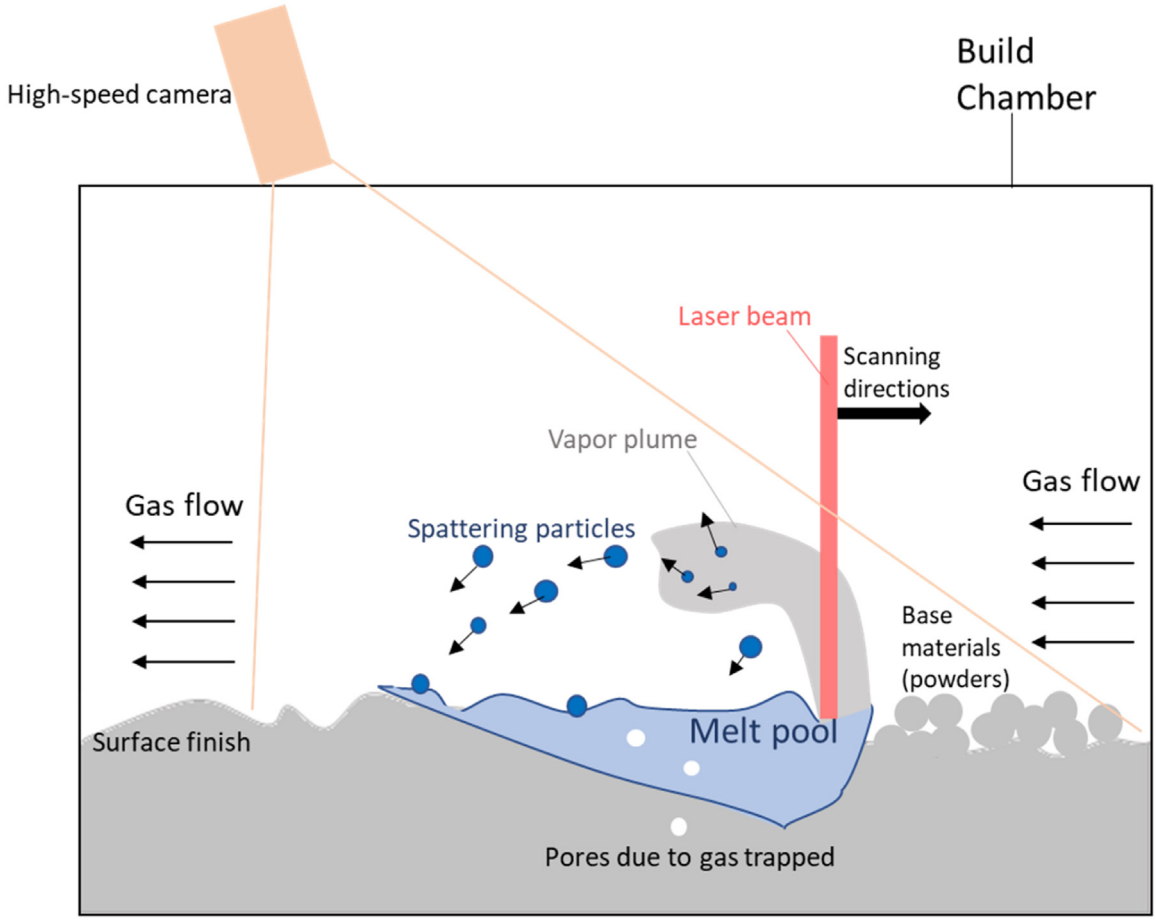

Fig. 5. A schematic diagram of the in-situ monitoring by the high-speed camera, with illustration of multi-physics phenomena during SLM process. It is a re-constructed diagram based on the multi-scale, multi-physics phenomena reported by Panwisawas et al. [35].

3. Results and discussion

3.1. SLM complexity and in-situ monitoring observations

Despite the extensive study of SLM over many years, its fundamental mechanics remain challenging to comprehend due to the intricate interplay of multiple physical phenomena across various length and time scales [35]. An example of this complexity is when the laser interacts with the metal powder, leading to the simultaneous interaction of all four states of matter: solid, liquid, gas (or vapour), and plasma, for which there are hardly any physics-based models available to tackle such complexity [35]. Given the complexity and high failure rate inherent in SLM, the implementation of in-situ monitoring throughout the process is important [36]. This allows for deeper insights into the procedure and facilitates prediction of the early-print quality, eventually saving both time and resources.

Fig. 5 presents the schematic diagram of in-situ monitoring via a high-speed camera used in this study with a frame rate of 460, and a time interval of 50 ms between two consecutive frames.The diverse multi-physics phenomena occurring during the SLM process are also illustrated in Fig. 5. SLM is performed within a build chamber filled with inert gas to minimise oxygen content. The inert gas aids in the removal of by-products generated during SLM, such as vapour plumes and spattered particles [37], counter to the laser scanning direction.

Fig. 6 shows screenshots of process signals at different time frames under varying laser power conditions. 0 s represents the start of the printing process, while 500 ms indicates the completion of printing for one sample. Two primary observations can be made in Fig. 6: the emergence of white spots and smoke during laser processing. White spots denote intensely heated objects, such as melt pools and spattered particles [9]. However, the size of these particles usually ranges from dozens to slightly over a hundred microns, falling below the resolution limit of the camera used in this study [38]. Consequently, the white spots (seen in Fig. 6) are identified as melt pools. The smoke observed represents vapour plumes, which are generated due to excessive energy input causing metal vapour.

3.1.1. Analysis of melt pool dynamics

During SLM, laser irradiation causes the metal powder to melt, forming a localised molten area known as the melt

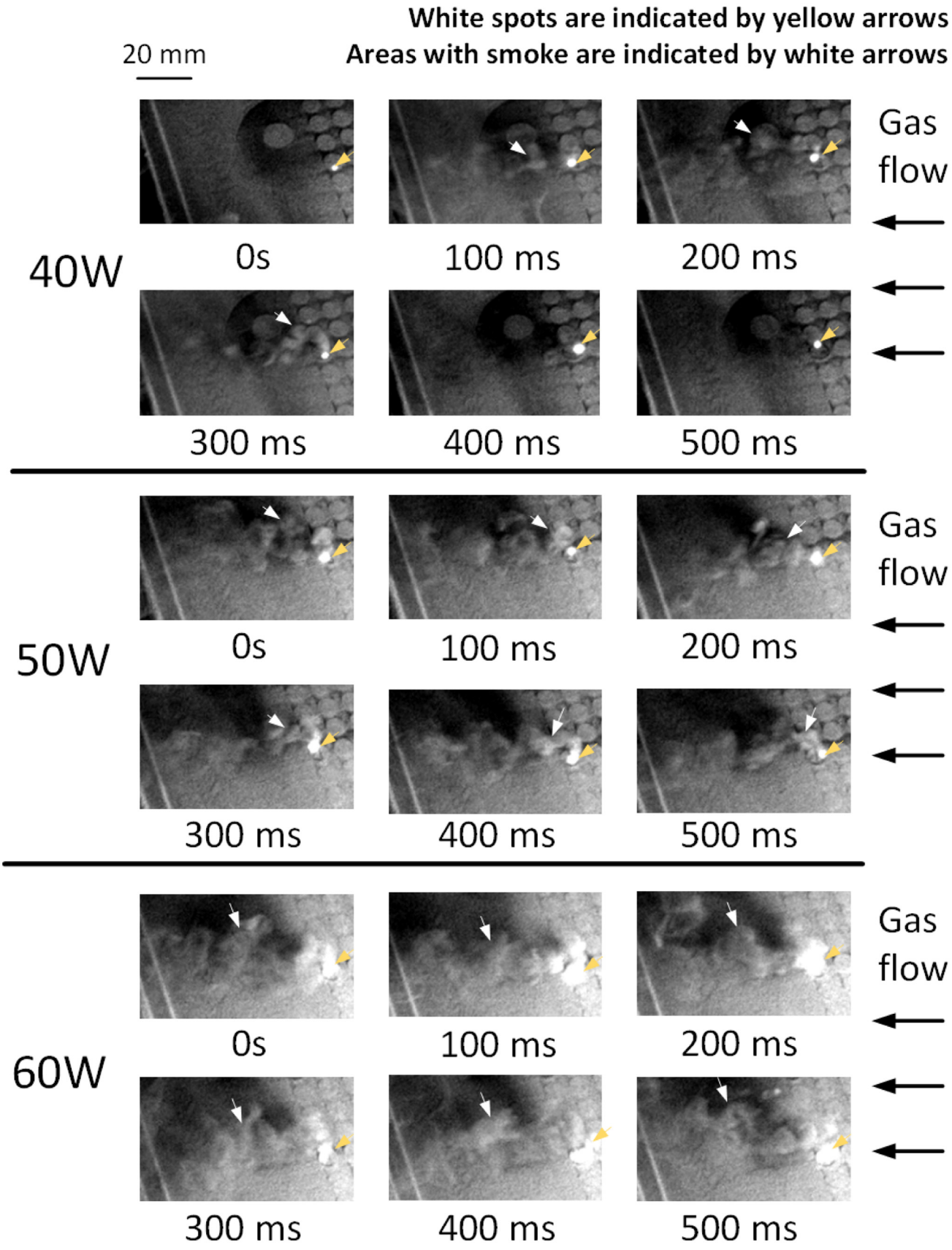

Fig. 6. Screenshots from high-speed camera videos of the SLM process showcase white spots and smoke at various time frames for laser powers ranging between 40 W and 60 W. The 0 s indicates the start of printing while the 500 ms indicates the completion of printing one sample.

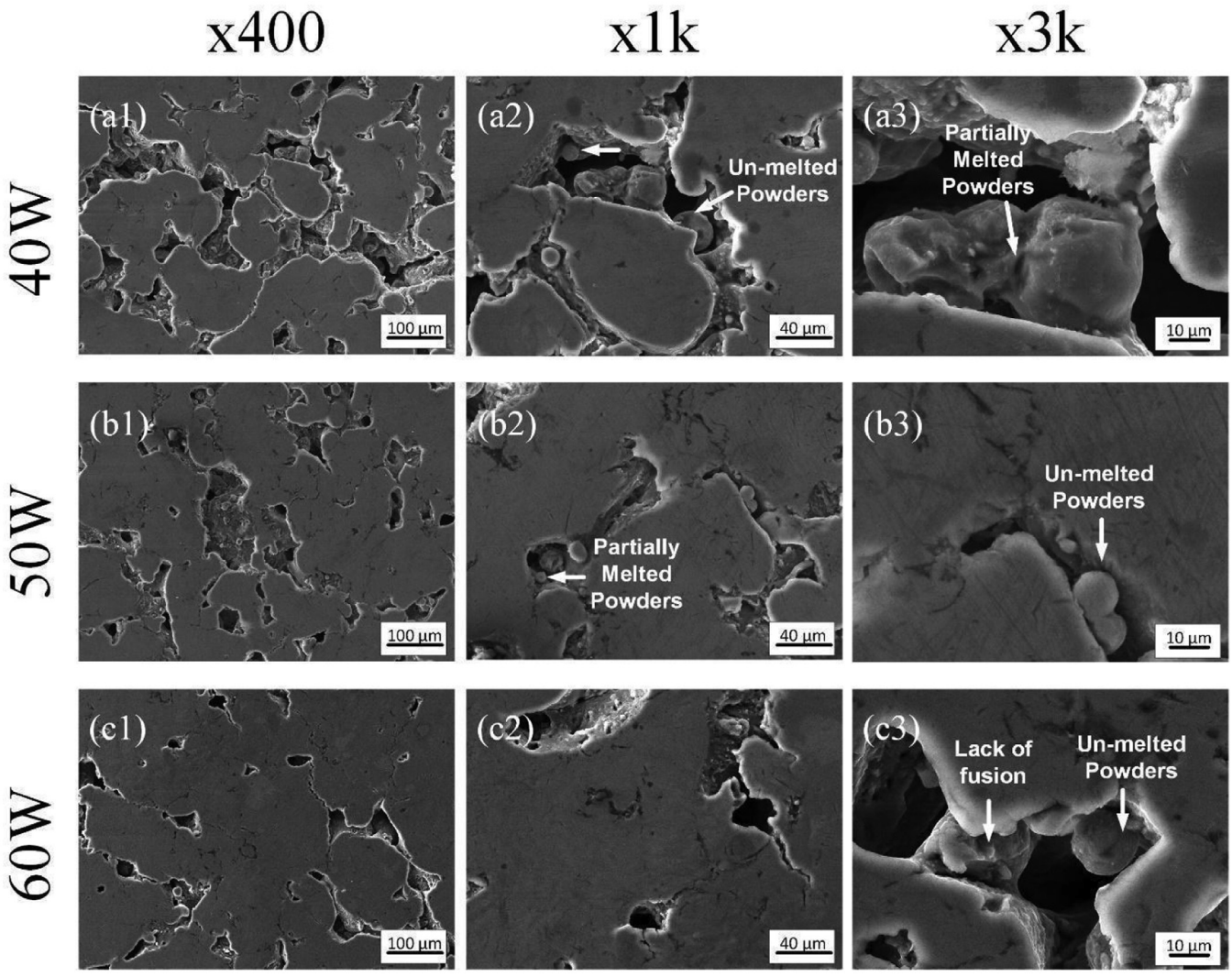

Fig. 7. SEM surface morphology of the Mg samples printed by the laser power of 40 W, 50 W, 60 W, respectively. The image magnifications are x400, x1k and x3k, respectively.

pool. This transient phenomenon, which involves rapid heating, melting, and solidification, is crucial to the properties of the printed part [10].

Commonly, high-speed cameras are utilised for capturing these dynamics, providing real-time visualisation of the process. However, these cameras, including the one used in this study, face limitations in capturing ultrafast transient events due to their spatial and temporal resolution constraints. Thus, the focus in this study is directed towards a more discernible feature of the melt pool which is based on its intense light emission (or the brightness of the white spot) to inform the melt pool size. This methodology is in line with the work conducted by Berumen et al. [26].

The number of white pixels (i.e., grey value equals 255) in each screenshot in Fig. 6 was recorded and averaged. The results revealed counts of 16.7, 23.2, and 59.7 for the laser powers of 40 W, 50 W, and 60 W, respectively. These results indicate that with an increase in laser power, the melt pool size expands, as evidenced by the increased brightness.

3.1.2. Analysis of vapour plume dynamics

Vapour plume dynamics, an integral part of the SLM process, has been analysed under different laser powers (Fig. 6). The observations show a noticeable change in the turbulence of the vapour plume, which is more laminar at 40 W and increasingly turbulent at 60 W.

The stronger turbulence at higher laser power is attributed to enhanced heat generation around the laser beam focal spot. This excess heat causes the surrounding gas to expand, inducing convection currents that contribute to the turbulence of the vapour plume [39]. Additionally, a higher laser power results in the vaporisation of more material, leading to an increase in the volume of the vapour plume. As a result, gases and particles within the vapour plume are ejected at increased ve-

localities and in larger volumes, leading to enhanced turbulence [40].

3.2. Surface morphology analysis of top surface by SEM

The top surface morphology of the samples produced at different laser powers is illustrated in the SEM images (in Fig. 7). Upon examination, the impact of laser power on pore formation and subsequent microstructure is evident. The samples of 40 W, 50 W and 60 W display pores of various shapes and sizes. Notably, an inverse relationship between laser power and pore coverage is observed, with lower laser powers resulting in higher pore coverages.

This trend becomes noticeable in the 40 W and 50 W samples, where un-melted and partially melted powders are more prominent. The presence of these un-melted and partially melted powders can be attributed to the lower energy inputs compared to the 60 W sample. Increased energy input, as observed at 60 W, can result in a denser component. This densification can be explained by the enhanced energy input at 60 W facilitating more complete melting of the metal powder. Such complete melting aids in eliminating microscopic pores, culminating in a denser material structure. However, the balance of energy input for the SLM-printed Mg alloy is delicate due to its inherently low melting and boiling points. Excessively high energy input, such as that beyond 60 W, could cause a rapid phase transition from solid/liquid to gas. Such phase transition could introduce defects, like cracks. To provide deeper insight and validate these observations, a detailed analysis of porosity using OM for the top and cross-sectional surfaces, and XC for the entire sample, will be presented in Sections 3.3, 3.4, and 3.5, respectively.

3.3. Porosity analysis on top surface by OM

3.3.1. Pore coverage analysis on top surfaces

Fig. 8(a1), (b1), and (c1) show the merged OM images for the samples of 40 W, 50 W, and 60 W, respectively. Their corresponding binary OM images, processed with the Otsu algorithm via ImageJ [27], are depicted in Fig. 8(a2), (b2), and (c2). Pore coverage measurements revealed that the 40 W, 50 W, and 60 W samples had the pore coverages of 20.5%, 15.6%, and 11.5%, respectively, suggesting an inverse relationship between laser power and pore coverage. This also implies that higher laser powers lead to more effective fusion of the powders, supporting the SEM observations presented in Fig. 7.

3.3.2. Pore size and morphology analysis on top surfaces

The Analyse Particles function in ImageJ enabled a thorough examination of pore size and morphology, providing individual identification and characterisation of each pore as illustrated in Fig. 8(a3), (b3), and (c3). Circularity is chosen as a parameter to evaluate pore morphology, with lower values signifying more irregularly shaped pores.

It is crucial to note that certain interconnected pores, characterised as pores linked with adjacent ones, can be identified using OM as illustrated in Fig. 8. However, due to the limitations inherent to ImageJ, these interconnected pores cannot be separately analysed. Therefore, they were not subjected to individual analysis.

The distributions of pore sizes and morphologies are shown in Fig. 9. Pores were grouped into three categories based on their size: small (<100 μm), intermediate (100-200 μm), and large (>200 μm). The smallest detectable pore size was 0.4 μm. The 40 W sample exhibited the smallest maximum pore size, while the 50 W sample had the largest. However, these distinctions are not depicted in Fig. 9(a1-c1) for visual clarity.

From the pore size distribution plots in Fig. 9(a1-c1), a total of 4641 pores were identified on the 40 W top surface, and the number increased to 5229 and 4853 on the 50 W and 60 W top surfaces, respectively. The smallest pores that can be identified from the 40 W to 60 W samples was 0.4 μm. Notably, the largest identifiable pore on the 40 W top surface (728.5 μm) was smaller than those on the 50 W top surface (966.9 μm) and 60 W top surface (865.3 μm). It should be noted that the maximum pore size does not display in Fig. 9(a1-c1) for viewing clarity too.

Despite the largest identifiable pore being smaller on the 40 W top surface, it cannot be inferred that the size of the largest pore on samples can be reduced by applying 40 W laser power as the porosity analysis was not conducted in three dimensions. This highlights a limitation of porosity analysis by OM. The pore size of the 40 W sample were the largest with a value of 40.9±69.2 μm, whereas that of the 50 W sample reduced to 34.6±59.3 μm and that of the 60 W sample further fell to 30.9±51.7 μm. On all samples, the majority of pores (about 90%) were of smaller sizes. Even though the percentage of intermediate-sized pores was similar in all samples, the total number of those pores decreased from 359 to 307 when the laser power increased from 40 W to 60 W. Additionally, the percentage of large pores was 4% (205 in total) on the 40 W sample. It declined to 3% (131 in total) and 2% (78 in total) on the 50 W and 60 W samples, respectively. It implied that the intermediate-sized and large pores can be reduced by increasing the laser power.

3.4. Porosity analysis on cross-sectional surface by OM

3.4.1. Pore coverage analysis on cross-sectional surfaces

Fig. 8(d1), (e1), and (f1) show the entire cross-sectional surfaces of the 40 W, 50 W and 60 W samples. The methodology used for image analysis of pore distribution, coverage, size, and morphology on the cross-sectional surfaces was the same as that used for the top surfaces. It is necessary to note that the samples were printed with the same thickness in the SLM process. However, a slight variance in the sample thickness was observed due to the settings of the wire-cut machine used to detach the samples from the substrate.

The smallest identifiable pore size on the cross-sectional surface was 0.4 μm. When comparing the pore coverage with the 50 W and 60 W samples, the 40 W sample exhibited the highest pore coverage (20.0%), which decreased to 14.2% on the 50 W sample and dropped to the lowest coverage of 9.4%

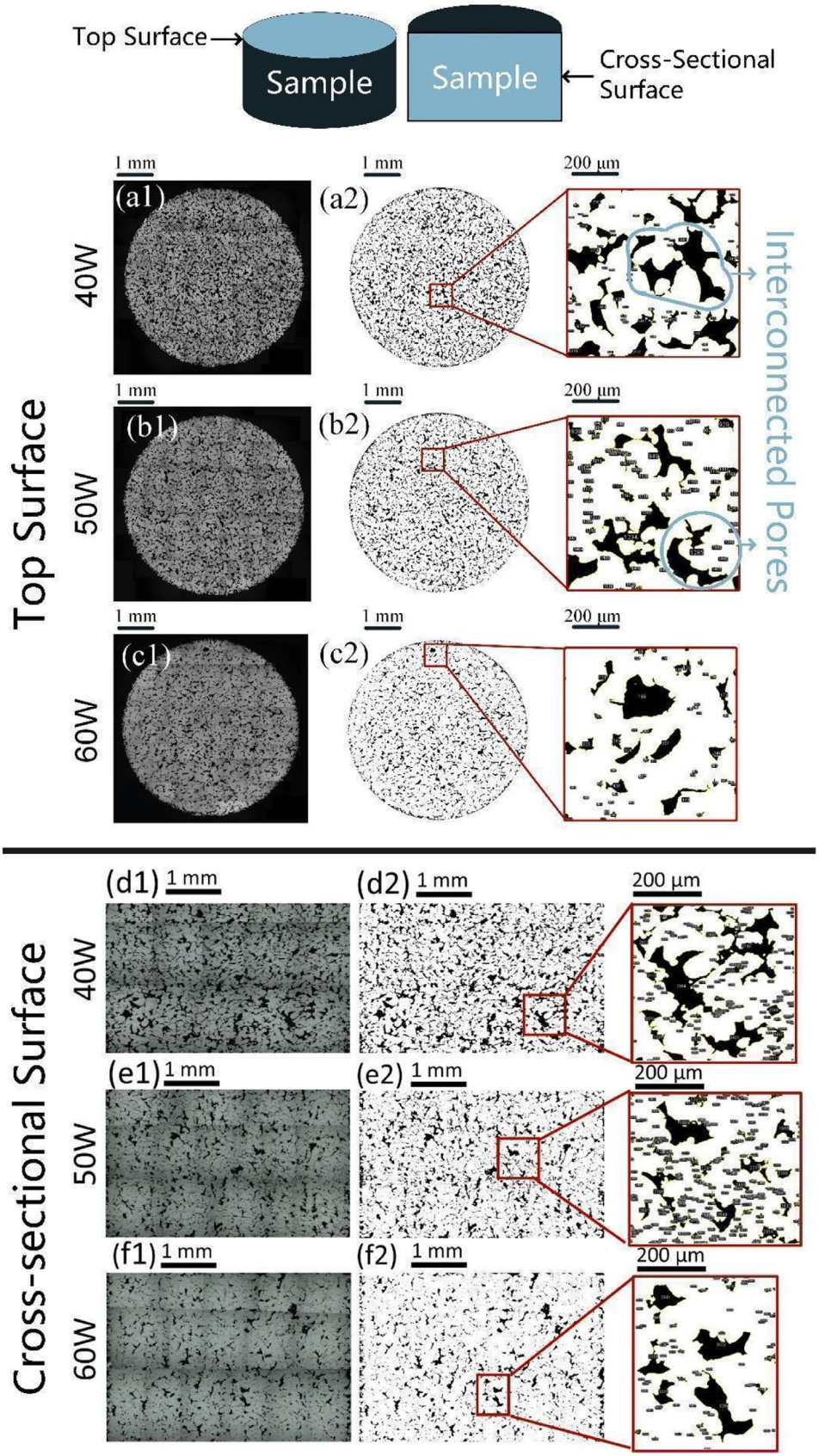

Fig. 8. OM porosity analysis on the top surfaces (a1-c2) and cross-sectional surfaces (d1-f2) at x50. (a1-f1), the merged OM images display the entire top or cross-sectional surfaces; (a2-f2) show the corresponding binary image for the pore coverage analysis; the magnified views of the pores identified using particle analysis function in ImageJ are highlighted in red.

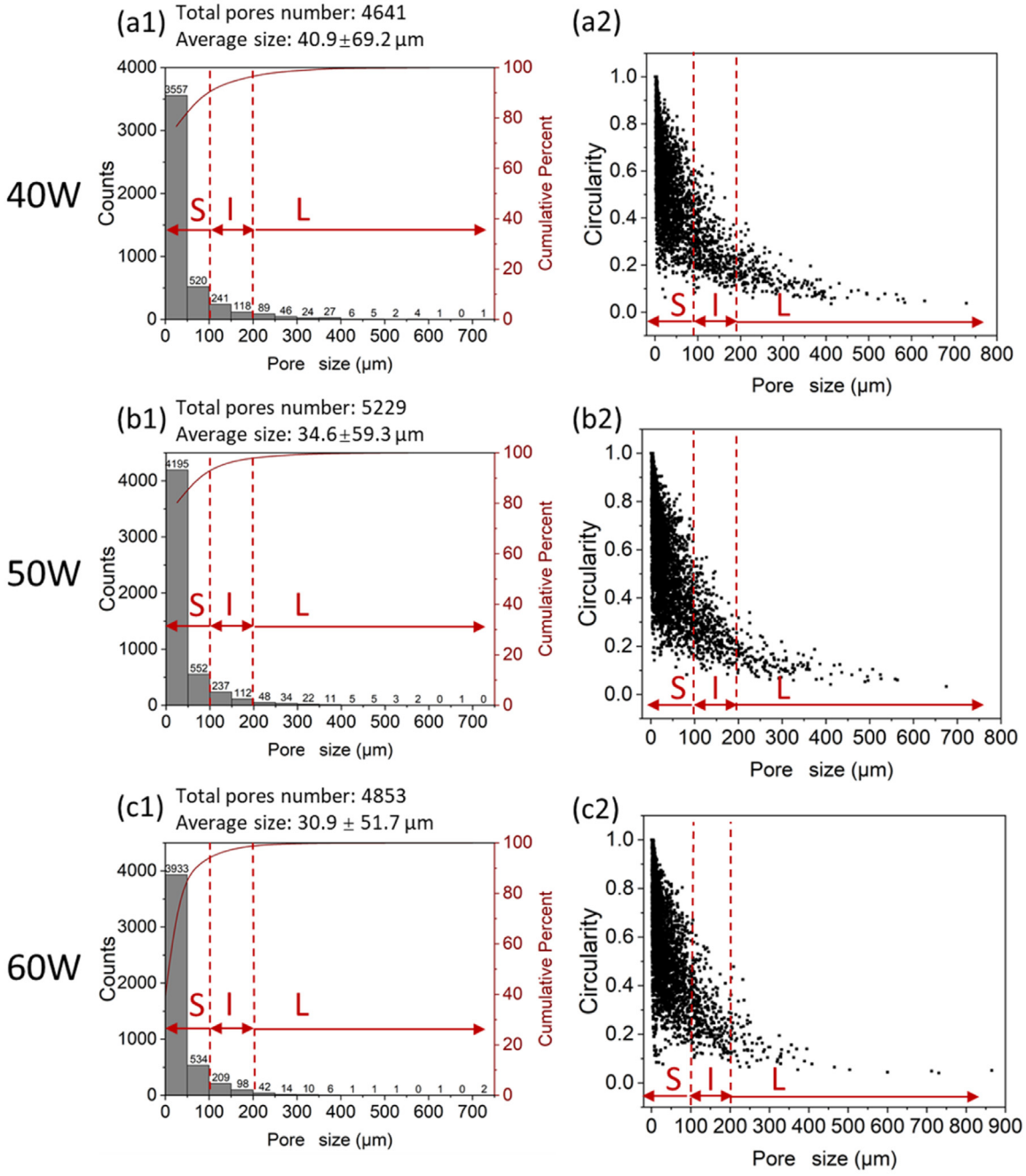

Fig. 9. OM pores statistics acquired from the top surfaces of 40 W, 50 W, and 60 W samples in Fig. 8 (a2), (b2) and (c2); the pore size distribution (a1, b1, and c1) and scatter plot of pore circularity as a function of pore size (a2, b2, and c2. Smaller pores (0-100 μm), intermediate-sized pores (100-200 μm), and larger pores (>200 μm) are denoted as S, I and L in this figure.

on the 60 W sample. Therefore, an increase in laser power at 60W can enhance the density of the samples.

3.4.2. Pore size and morphology analysis on cross-sectional surfaces

As demonstrated in the pore size distribution graphs in Fig. 10(a1-c1), a total of 4001 pores were detected on the 40 W cross-sectional surface, with 5343 and 4378 pores observed on the 50 W and 60 W cross-sectional surfaces, respectively. Regarding pore size, the maximum identifiable pore size on the 40 W sample was 601.5 μm, while it was 364.8 μm on the 50 W sample and 412.6 μm on the 60 W sample. The smallest identifiable pores (0.4 μm) were found in all samples, irrespective of the laser power applied. The 40 W sample had the largest pore size, measuring at 26.6±48.6 μm. This pore size in the 50 W sample decreased to 19.0±33.6 μm, and for the 60 W sample, it dropped further to 18.2±31.6 μm. The majority of pores (i.e., > 90%) were of small sizes (<100 μm). In the 40 W sample, there was a notable presence of intermediate-sized pores (100-200 μm) and large pores

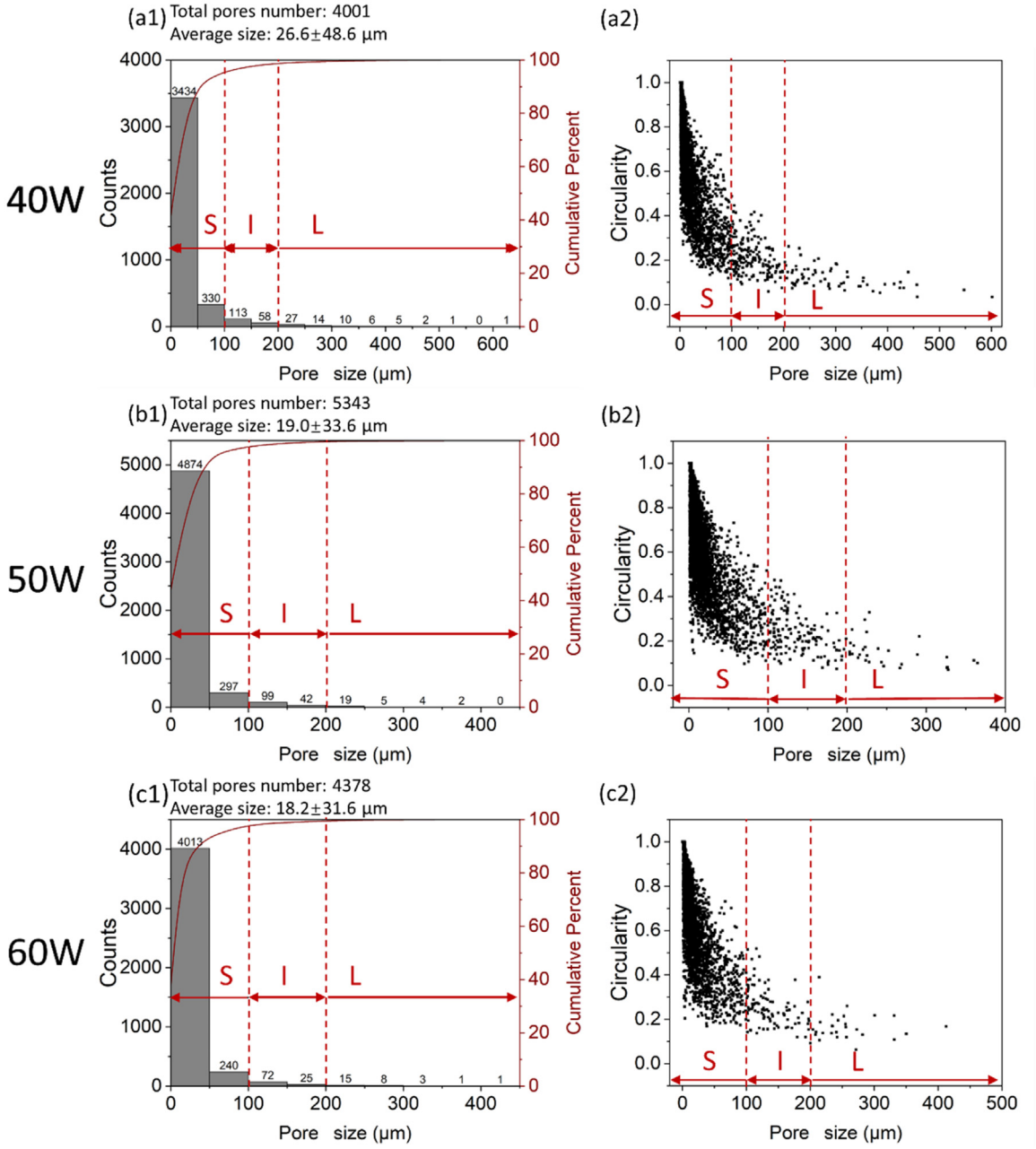

Fig. 10. OM Pores statistics acquired from the cross-sectional surfaces of 40 W, 50 W, and 60 W samples in Fig. 8 (d2), (e2) and (f2); the pore size distribution (a1, b1, and c1) and scatter plot of pores circularity as a function of pore size (a2, b2, and c2). Smaller pores (0-100 μm), intermediate-sized pores (100-200 μm), and larger pores (>200 μm) are denoted as S, I and L in (a1-c1).

(>200 μm), with counts of at 171 and 66 respectively. As the laser power increased, the count of both intermediate-sized and large pores decreased, with the 60 W sample having the fewest at 97 for intermediate-sized pores and 28 for large pores.

Regarding pore morphology, only a few smaller pores exhibited a circularity below 0.2. In contrast, intermediate-sized and large pores showed a circularity ranging from 0.1 to 0.4 and 0.1 to 0.3, respectively. This trend agrees with the observations from the top surfaces, where pores exceeding 100 μm predominantly exhibited irregular shapes.

In summary, the findings from the pore analysis of the cross-sectional surfaces correspond with those of the top surfaces. Increasing the laser power appears to reduce pore coverage, pore size, and the occurrence of intermediate and large pores. Pores exceeding 100 μm predominantly exhibited irregular shape, while circular pores (with a circularity exceeding 0.8) were largely confined to those smaller than 50 μm. It is important to highlight that, irrespective of the laser power applied, the pore size on the cross-sectional surfaces was consistently smaller than on the top surfaces.

Table 2
Summary of pore characteristics in different samples analysed by XCT.

	Pore type	Number	Volume, mm^3	Volume fraction (or pore coverage), %
40 W	Isolated	219	0.01	0.01
	Interconnected	—	10.98	18.12
	Overall	—	10.99	18.13
50 W	Isolated	495	0.02	0.03
	Interconnected	—	10.68	15.22
	Overall	—	10.7	15.25
60 W	Isolated	1545	0.21	0.44
	Interconnected	—	4.27	8.89
	Overall	—	4.48	9.33

3.5. Porosity analysis using XCT

3.5.1. Brief introduction to XCT for porosity analysis

XCT is a non-destructive method that is popular in both academia and industry for its rapid scanning capabilities. After the samples are scanned and data is reconstructed, a 3D representation of their internal structure is created (shown in Fig. 11), facilitating a thorough 3D porosity analysis.

3.5.2. Identification of pore types and their analysis

In the samples, as depicted in Fig. 11(a1-c1), nearly all the pores appeared to be interconnected, suggesting a connection to adjacent pores. These interconnected pores are highlighted in red and will be referred to as "interconnected pores" throughout this analysis. Alongside these, isolated pores were also observed in each sample. To ensure a structured analysis, the XCT porosity analysis was segmented into two parts: (i) the overall porosity analysis, which encompasses both isolated and interconnected pores, and (ii) the isolated porosity analysis which focuses only on the isolated pores while omitting the interconnected ones. A schematic diagram representing this categorisation is depicted in Fig. 11. The data detailing the count, volume, and volume fractions for each pore type (isolated, interconnected, and overall) is summarised in Table 2.

3.5.3. Overall porosity analysis

The XCT porosity analysis reveals pore coverage of 18.13%, 15.25%, and 9.33% for the 40 W, 50 W, and 60 W samples, respectively. For these samples, the smallest identifiable pores were 17.7 μm, 12.5 μm, and 13.6 μm, respectively. These values are notably larger than the theoretical XCT resolution threshold of 9.3 μm, as mentioned in Section 2.5. It is important to note that the OM method, as described in Sections 3.3 and 3.4, can detect pores that are smaller than the aforementioned limit. Therefore, utilising a combination of XCT and OM imaging techniques can enable a more thorough and comprehensive evaluation of the sample porosity.

3.5.4. Interconnected and isolated porosity analysis

The interconnected porosity analysis demonstrated that the samples subjected to 40 W and 50 W have considerably larger interconnected pore volumes, amounting to 10.98 mm^3 and 10.68 mm^3 respectively. These volumes equate to pore coverages of 18.12% and 15.22%. In contrast, the 60 W sample exhibited a smaller volume of 4.27 mm^3, corresponding to a pore coverage of 8.89%. Given the intricate nature of interconnected pores, a simple count is insufficient for representation. Their volume serves as a more indicative measure.

After extracting the interconnected pores, the number and volume of isolated pores were measured and analysed for each sample. Fig. 11 (a2-c2) shows the cross-sectional views of these isolated pores, while their top views are presented in Fig. 11(a3-c3). The samples of 40 W, 50 W, and 60 W had 219, 495, and 1545 isolated pores, leading to volumes of 0.01 mm^3, 0.02 mm^3, and 0.21 mm^3, respectively. These volumes correspond to the pore coverages of 0.01%, 0.03%, and 0.44%, respectively.

When comparing the 60 W sample to its 40 W and 50 W counterparts, there is a noticeable increase in the number of isolated pores spread throughout the 60 W sample. However, the concentration of these pores in the central region reduced. This observation could be a result of the increased energy from the 60 W laser, enabling a more complete melting process, and thus promoting a more even redistribution of material. Such even redistribution could lead to a more consistent dispersal of isolated pores across the sample. The lower concentration of isolated pores in the central region may be due to higher cooling rates compared to the periphery. The rapid cooling could prevent the formation of extensive interconnected pore networks and subsequently result in the predominance of isolated pores.

In addition, isolated pores with the size larger than 200 μm were primarily located at the periphery of the 60 W sample, as indicated by the pores coloured with green, orange, and red in Fig. 11(c3). This finding suggests that heat accumulation at the edges, a phenomenon commonly observed in laser-based manufacturing processes due to slower heat dissipation, could promote the formation of larger pores. Rapid solidification under higher temperatures might lead to these large pores as gases or volatile elements are entrapped.

Although the 60 W sample exhibited a higher number of isolated pores, their concentration in the central region was found to be reduced. However, the underlying factors driving this discrepancy remain inconclusive, necessitating further investigations in future studies.

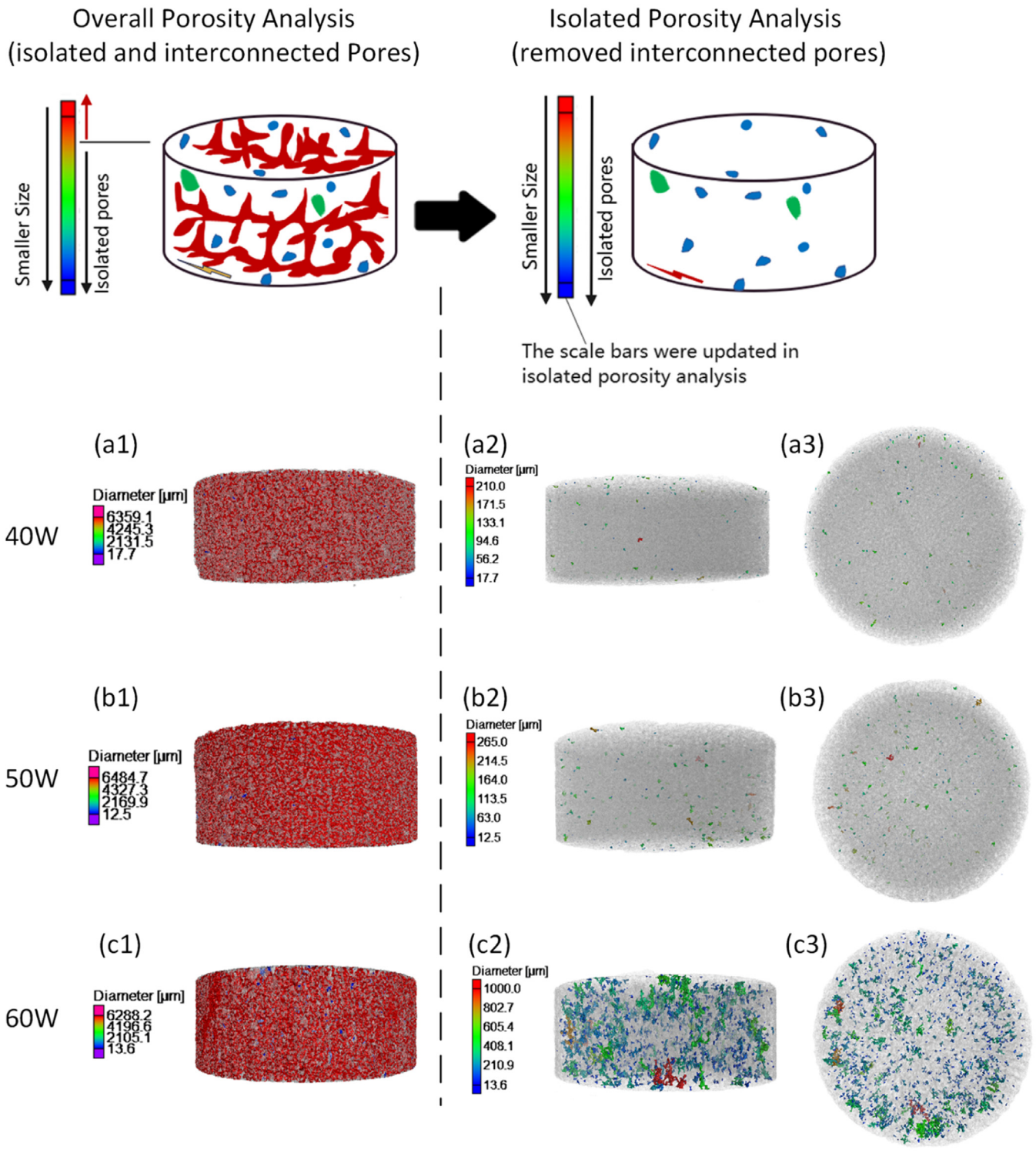

Fig. 11. XCT porosity analysis of the 40 W, 50 W, and 60 W samples provided with schematic diagrams to aid the visualisation of pore types: (a1), (b1) and (c1) include both isolated and interconnected pores, while (a2-c3) include only the isolated pores. The scales in this figure reflect variations in pore size distribution across different samples. As such, the colour-coded representation of pore sizes is specific to each individual sample.

3.5.5. Pore size distribution, sphericity, and aspect ratio

In the SLM-printed Mg samples, both sphericity and aspect ratio metrics are used to characterise the isolated pore shape. Sphericity measures pore regularity, with pores registering a sphericity higher than 0.6 being categorised as "near spherical". Conversely, those with a sphericity less than 0.6 are termed "irregular". From this irregular category, pores with an aspect ratio higher than 2 are identified as "elongated". The aspect ratio, determined by the ratio of maximum to minimum pore diameter, offers insight into pore elongation. It is

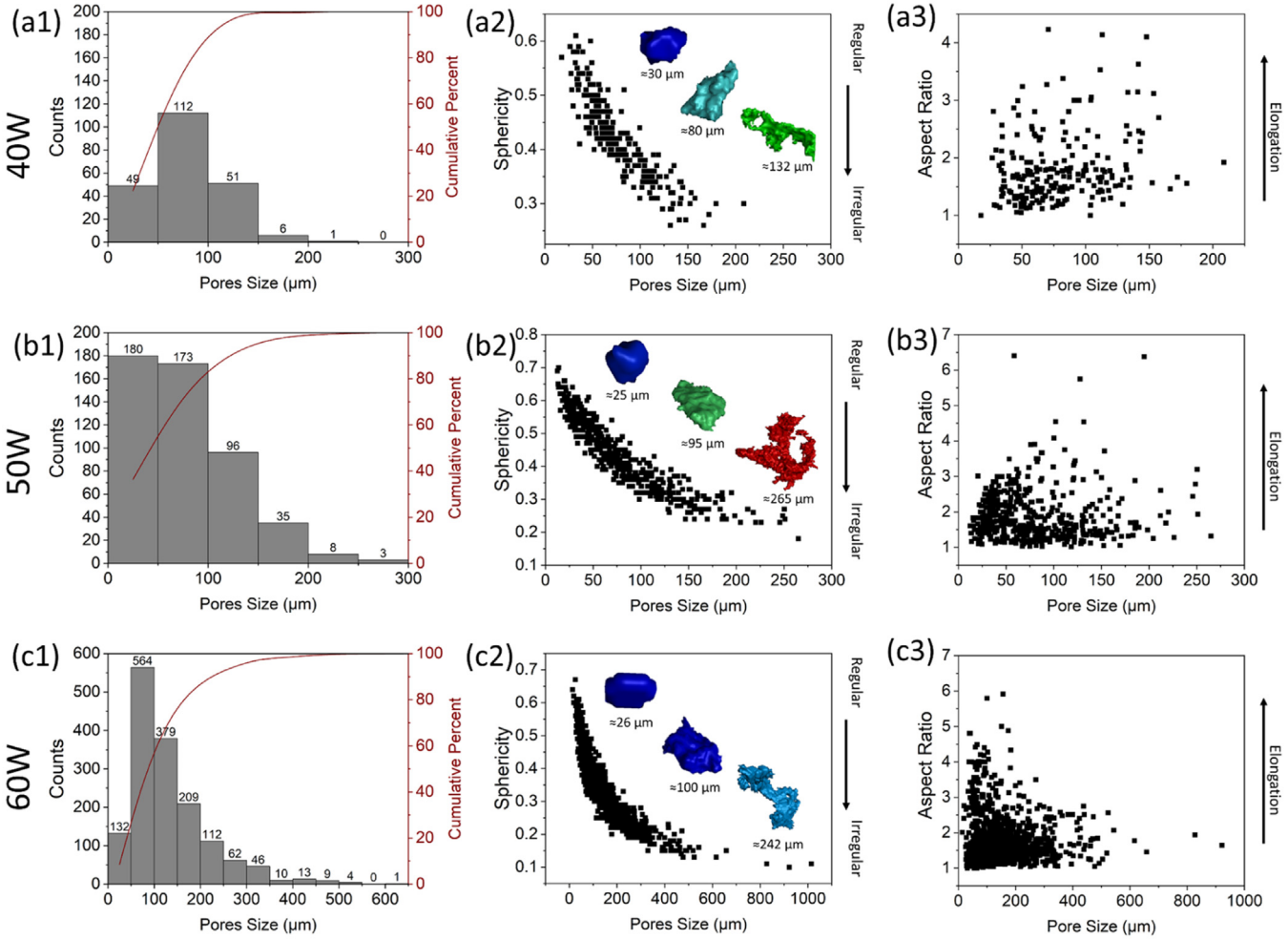

Fig. 12. XCT pore statistics acquired from the 40 W, 50 W and 60 W samples in Fig. 11 (a2-c2); the pore size distribution (a1, b1, and c1), scatter plot of pore sphericity as a function of pore size (a2, b2, and c2) and scatter plot of pore aspect ratio as a function of pore size (a3, b3 and c3).

noteworthy that elongated pores tend to be more vulnerable to localised stress concentrations during stretching, a finding supported by [17].

The distribution graphs of pore size, as well as the scatter plots of pore sphericity and aspect ratio as a function of pore size for different samples are presented in Fig. 12. Most isolated pores on all samples exhibited an irregular shape, with a sphericity lower than 0.6, as depicted in Fig. 12(a2-c2). Generally, sphericity decreased with increasing pore size. Such observations indicate that pore size does not necessarily dictate its aspect ratio, as evident from Fig. 12(a3-c3). Even smaller pores can manifest a high aspect ratio. The samples consistently revealed elongated pores, with an aspect ratio > 2.

The XCT analysis indicated that at 40 W and 50 W, the interconnected pores constituted over 99% of the total pore volume, while at 60 W, they decreased to 95% due to an increase of the isolated pores. It is important to note that such interconnected pores could significantly influence the degradation performance of Mg alloys compared to isolated pores. This can be attributed to their inherent spatial arrangement, fostering a wide network conductive to molecular interactions.

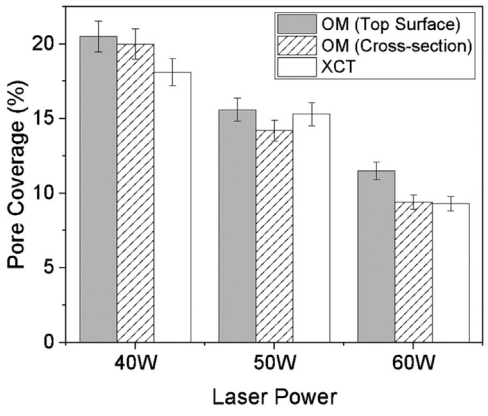

Fig. 13. Comparison of average pore coverages between the OM and XCT measurements across different samples. The error bars indicate n=3.

3.5.6. Comparative analysis between OM and XCT

The bar chart in Fig. 13 shows the average pore coverages across different samples, as determined through the OM and XCT porosity analysis conducted in Sections 3.4 and 3.5, respectively. Apart from the 50 W cross-sectional surface,

Table 3
Variations in pore sizes as measured by OM and SEM. The pores were captured from the top surfaces of different samples and their variations were represented by error percentages.

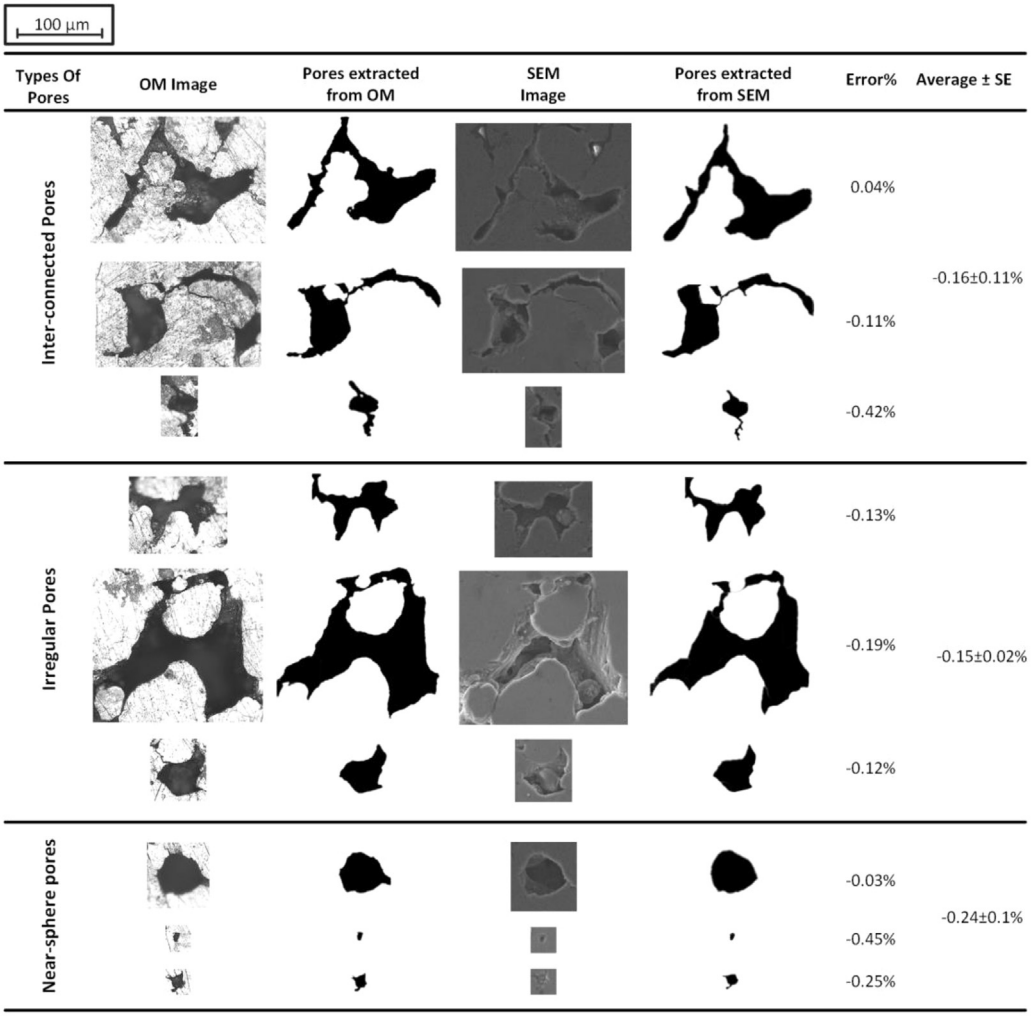

the average pore coverages identified by OM were generally higher than those identified by XCT. However, it is worth noting that the difference is not substantial, with OM indicating slightly higher percentages.

Such difference can be attributed to the resolution differences between the two imaging techniques. The superior resolution of OM, reaching up to 0.4 μm, allows it to detect finer details, resulting in the identification of a higher number of pore. On the other hand, the resolution of XCT is limited to details larger than 9.3 μm. Therefore, the ability of OM to detect and quantify smaller pores, which fall below this XCT resolution threshold, is an important factor contributing to this observed variance.

Comparing both methods emphasises the synergistic benefits of using XCT and OM together to achieve a more comprehensive analysis of porosity in the SLM process. XCT offers a non-destructive approach for 3D analysis of the samples, revealing internal structures. In contrast, OM offers detailed 2D insight at a higher resolution. Therefore, by combining XCT and OM, one can obtain a comprehensive perspective on the porosity, capturing insights into pore sizes, spatial arrangement and their interrelationships.

3.6. Error analysis of OM measurements

The accuracy of porosity analysis via OM images can be influenced by several factors: (1) the optical resolution of microscope, (2) potential optical aberrations that might distort the image, (3) the resolution of camera and subsequent digitisation of the image [41], and (4) the algorithm employed by the image analysis software. It is worth noting that the inherent optical aberrations in microscopy can introduce errors, potentially influencing the accuracy of the porosity analysis.

For error assessment, nine distinct pores were selected: three each from interconnected, irregular, and near-sphere categories, for comparison between OM and SEM imaging techniques. SEM was chosen for this comparative analysis due to its outstanding resolution, larger depth of field, and enhanced capabilities in distinguishing surface and material contrasts [42], which can contribute to a more precise measurement

of pore sizes. The results of this analysis are presented in Table 3. The error percentage was calculated using the following equation:

$$Error\% = \frac{A_{SEM} - A_{OM}}{A_{SEM}} \times 100\%$$

Where A_{OM} is the area of each pore as measured from the OM image, and A_{SEM} is the area of the corresponding pore as captured in the SEM image.

Overall, the error percentages in Table 3 ranged from -0.03% to -0.45% with an average value of -0.18 ± 0.16%. When examining the error percentages by pore type: the interconnected pores showed the average error of -0.16 ± 0.11%, whilst the average errors of the irregular pores and the near-sphere pores were found to be -0.15 ± 0.02%, and -0.24 ± 0.10%, respectively. No significant difference in error percentages were observed across these pore categories. In this context, a negative percentage indicates the pore size measured by OM was larger than that measured by SEM. Except for one interconnected pore, all other measurements yielded negative percentages, suggesting that the pores measured by OM were consistently larger than those obtained from SEM.

3.7. Implications of process signals captured by high-speed cameras on porosity

3.7.1. Effect of melt pool size on porosity

In general, the influence of the melt pool size on porosity is indirect but important. A larger melt pool primarily indicates enhanced fusion between metal powders, effectively reducing porosity. This reduction in porosity stems from the stronger cohesion and integration of the particles within the larger melt pool, leading to a more solid, compact, and thereby less porous final product.

However, an excessively large melt pool can have its own issues. When the melt pool is too large, it may cause the collapse of the molten material. This collapse occurs because the structural integrity of the larger melt pool can be compromised due to the lack of sufficient supporting material around it, causing a collapse into the void space and the subsequent formation of porosity [43].

The optimal balance between these two factors: sufficient fusion and melt pool collapse, therefore plays a crucial role in controlling the level of porosity in the printed Mg parts, underlining the importance of carefully controlling the melt pool size during the SLM.

3.7.2. Effect of vapour plume on porosity

The vapour plume generated during SLM has significant implications for the porosity of the Mg samples. During the laser-powder interaction, material vaporisation gives rise to a plasma, which forms a plume above the melt pool. This plume applies localised pressure (or recoil pressure) to the liquid material potentially introducing environmental gas into the melt pool, a process which can contribute to porosity [44,45].

The degree of turbulence within the vapour plume plays a crucial role in the extent of this gas intrusion. A more turbulent vapour plume, as observed in the 60 W sample, implies increased localised pressure, thus increasing the chances of environmental gas intrusion into the melt pool and subsequently, higher porosity. However, in the case of the 60 W sample, the higher laser power increases the temperature of the melt pool, leading to lower viscosity [25]. This reduction in viscosity helps the entrapped gas coalesce and escape before the melt pool solidifies, thereby reducing the porosity [25]. This suggests that although a more turbulent vapour plume may potentially lead to increased porosity, other factors, such as the energy input from the laser, can counteract this effect.

3.7.3. Essential high-speed camera specifications for in-depth analysis of SLM melt pool and vapour dynamics

For an in-depth analysis of melt pool dynamics and vapour plume behaviour, spatial resolution is a critical parameter. The ideal camera should be capable of obtaining images at a resolution where each pixel corresponds to dozens of micrometres. Such high spatial resolution is essential for capturing subtle variations in the melt pool as well as the details of vapour plume behaviour. Temporal resolution, defined by the frequency at which images are captured, holds significance equivalent to spatial resolution. Given the rapid progression of events within the SLM process, a camera with a frequency exceeding 1000 Hz is recommended, as indicated by Grasso et al. [46]. Frame rates of this magnitude are crucial to ensure an accurate representation of real-time events and deviations in both melt pool dynamics and vapour plume behaviour during the SLM process.

3.8. Porosity and its impact on material properties

The relationship between the characteristics of pores (specifically volume fraction, type, size, shape, and location) and the material properties in SLM is intricate and multifaceted. Generally, materials with a higher volume fraction of pores have more porous space, which can lead to diminished mechanical strength and increased susceptibility to corrosion. In terms of pore types, interconnected pores present a greater risk for localised degradation when compared to isolated pores. This is because they offer a more extensive channel for fluids, thereby elevating the risk of propagating corrosion throughout the material.

Regarding pore size and shape, larger pores are conventionally viewed as more detrimental than their smaller counterparts. Furthermore, pores that are irregular and elongated can become focal points for stress, resulting in compromised mechanical attributes such as tensile and fatigue strength [17]. Concerning pore location, Al-Maharma et al. [47] reported that pores located near the surface regions determined the initiation of fatigue damage and the initial corrosion rate of materials. In addition, they found that pores located between the deposited layers have a strong and decisive influence on the toughness properties of materials when the load is applied

Table 4
Pore characteristics: comparison of Mg alloy with SLM-printed Ti-6Al-4V and 316L.

Type of alloy	Specific alloy	Percentage of irregular pores	Publication year [Reference]
Mg alloy	ZK60	>95%	This work
	Ti-6Al-4V	<50%	2020 [17]
		<5%	2022 [18]
		<20%	2019 [19]
		<5%	2021 [20]
		<5%	2023 [49]
		<50%	2022 [50]
		<10%	2022 [51]
		<5%	2021 [52]
Stainless steel	316L	<80%	2014 [21]
		<50%	2019 [27]
		<10%	2021 [53]

transverse to the layer direction, since these defects lead to delamination between the deposited layers.

It is essential to note that the specifics of how these pores impact on properties can be different based on the type of material being processed. For example, while stainless steels may maintain higher corrosion resistance even with larger pores, Mg alloys could exhibit pronounced degradation in the presence of similar porosity. Furthermore, research by Du Plessis et al. [48] suggests that pores below a certain critical size, such as 50 μm, might not have a substantial impact on the mechanical properties of the material. However, this critical pore size is material dependent. For instance, while it may be 50 μm for ZK60 Mg, it could be 200 μm for stainless steel. Given these variations, there is a need for more detailed investigation in the future to better understand the relative significance of pore size across different materials.

3.9. Pore characteristics: comparison of Mg alloy with SLM-printed Ti-6Al-4V and stainless steel 316L

Compared to the commonly-used alloys printed by SLM in the literature, namely 316L [21,23,41] and Ti-6Al-4V [17-20,49-52], Mg alloy exhibited a notably higher prevalence of irregular pores (sphericity < 0.6). As detailed in Table 4, this alloy displayed over 95% irregularity. Several inherent factors in Mg alloys contribute to this notable difference. Firstly, the distinct solidification dynamics of Mg, combined with its increased intrinsic reactivity, can lead to gas entrapment or atmospheric reactions during the SLM process [54]. Secondly, the higher thermal conductivity of Mg can result in rapid and uneven cooling during the SLM process [54], further contributing to the formation of irregular pores. Lastly, the grain structure and morphology of SLM-printed Mg are significantly different from those of 316L and Ti-6Al-4V [54], with grain boundaries potentially acting as initiation sites for defect formation [55].

4. Conclusions

In the SLM process, multi-physics phenomena introduce certain complexities. Utilising a high-speed camera, this study captured the real time dynamics of melt pools and vapour plumes under varying laser power settings. It was observed that an optimal balance between sufficient fusion and melt pool collapse is essential for managing porosity in the SLM process. Furthermore, the turbulence level of the vapour plume, paired with laser energy input, can influence the incorporation of environmental gases into the melt pool. This directly affects the porosity of the SLM-printed Mg parts.

The microscopic investigations using OM and SEM indicate that increasing laser powers from 40 W to 60 W can lead to a denser structure (i.e., reduction in pore coverage). The OM results also suggest the size of pores larger than 100 μm can be effectively reduced by applying the laser power of 60 W. For all samples, pores less than 50 μm in size are primarily observed to be nearly circular, with a circularity above 0.8. On the contrary, pores larger than 100 μm predominantly exhibit irregular shapes.

In addition to the OM 2D images, XCT provided a 3D perspective of the Mg samples. The XCT results indicate that the interconnected pores constitute over 99% of the total pore volume for the 40 W and 50 W samples. In contrast, increasing the laser power to 60 W appears to promote the formation of isolated pores, resulting in a reduction of interconnected pores to 95%. It should be noted that a small discrepancy was observed between the XCT and OM results. This could be attributed to the difficulty of XCT in detecting finer pores that fall below its resolution threshold (< 9.3 μm).

Finally, the OM method employed in this study allows the capture of full-surface images, presenting a potentially cost-effective and precise method for assessing porosity in the SLM process. This OM method can serve as an alternative approach to XCT without compromising the quality of porosity analysis.

Declaration of competing interest

The authors declare that they have no known competing financial interests or personal relationships that could have appeared to influence the work reported in this paper.

CRediT authorship contribution statement

Weijie Xie: Data curation, Formal analysis, Investigation, Writing – original draft. **Hau-Chung Man:** Conceptualization, Funding acquisition, Supervision, Writing – review & editing. **Chi-Wai Chan:** Data curation, Investigation, Methodology, Writing – review & editing.

Acknowledgement

The work described in this paper was fully supported by a grant from the Research Grants Council of the Hong Kong Special Administrative Region (152131/18E). Support from the infrastructure of The Queen's University Belfast, The Hong Kong Polytechnic University and University Research Facility in 3D Printing(U3DP) is also acknowledged.

References

[1] M. Ahmadi, et al., J. Mater. Res. Technol. 19 (2022) 1537–1562.
[2] T. Kurzynowski, A. Pawlak, I. Smolina, Arch. Civil Mech. Eng. 20 (1) (2020) 23.
[3] Y.Q. Zhang, et al., Orthop. Surg. 10 (2) (2018) 160–168.
[4] C.L. Wu, W. Zai, H.C. Man, Mater. Today Commun. 26 (2021) 101922.
[5] Q. Deng, et al., Addit. Manuf. 49 (2022) 102517.
[6] Q. Deng, et al., Mater. Charact. 165 (2020) 110377.
[7] Q. Deng, et al., Mater. Charact. 190 (2022) 112071.
[8] C. Gao, et al., J. Magnes. Alloys 9 (1) (2021) 305–316.
[9] X. Lin, et al., J. Mater. Process. Technol. 303 (2022) 117523.
[10] B. Gould, et al., JOM 73 (1) (2021) 201–211.
[11] H. Gong, et al., Mater. Des. 86 (2015) 545–554.
[12] R. Biswal, A.K. Syed, X. Zhang, Addit. Manuf. 23 (2018) 433–442.
[13] J. Stef, et al., Mater. Des. 156 (2018) 480–493.
[14] J. Suryawanshi, et al., Materialia 3 (2018) 153–161.
[15] G. Wang, et al., J. Alloys Compd. 831 (2020) 154815.
[16] D. Yang, et al., Appl. Phys. A 128 (1) (2021) 51.
[17] W. Liu, et al., Mater. Sci. Eng.: A 797 (2020) 139981.
[18] X. Yan, et al., J. Manuf. Process. 77 (2022) 151–162.
[19] T. Mishurova, et al., Addit. Manuf. 25 (2019) 325–334.
[20] J. Ge, et al., Mater. Des. 198 (2021) 109292.
[21] G. Ziółkowski, et al., Arch. Civil Mech. Eng. 14 (4) (2014) 608–614.
[22] S.M. Yusuf, et al., Metals 7 (2017), doi:10.3390/met7020064.
[23] H. Choo, et al., Mater. Des. 164 (2019) 107534.
[24] K. Solberg, et al., Fatig. Fract. Eng. Mater. Struct. 42 (9) (2019) 2043–2052.
[25] S. Tammas-Williams, et al., Mater. Charact. 102 (2015) 47–61.
[26] S. Berumen, et al., Phys. Procedia 5 (2010) 617–622.
[27] J. Yousefi, Image Binarization Using Otsu Thresholding Algorithm, 2015.
[28] F.Y. Yap, et al., Diagn. Interv. Radiol. 19 (2) (2013) 97–105.
[29] M.A. Ali, et al., Compos. Sci. Technol. 184 (2019) 107828.
[30] S.R. Stock, Int. Mater. Rev. 53 (3) (2008) 129–181.
[31] E. Maire, P.J. Withers, Int. Mater. Rev. 59 (1) (2014) 1–43.
[32] A. Delesse, Ann. Min. (IV) 13 (1848) 379–388.
[33] B.M. Patterson, et al., Microsc. Microanal. 18 (2) (2012) 390–398.
[34] M. Pavan, et al., Polym. Test. 66 (2018) 203–212.
[35] C. Panwisawas, Y.T. Tang, R.C. Reed, Nat. Commun. 11 (1) (2020) 2327.
[36] Y. AbouelNour, N. Gupta, Mater. Des. 222 (2022) 111063.
[37] W. Xie, et al., J. Laser Appl. 35 (2) (2023) 022019.
[38] D. Wang, et al., Mater. Des. 117 (2017) 121–130.
[39] J.P. Oliveira, T.G. Santos, R.M. Miranda, Prog. Mater Sci. 107 (2020) 100590.
[40] J. Liu, P. Wen, Mater. Des. 215 (2022) 110505.
[41] R.A. Carlton, S. Englehart, Microsc. Microanal. 11 (S02) (2005) 1248–1249.
[42] M. Sato, et al., Nucl. Instrum. Methods. Phys. Res. A 519 (1) (2004) 280–285.
[43] B. Liu, G. Fang, L. Lei, Appl. Math. Modell. 92 (2021) 505–524.
[44] T. Cullom, et al., Sci. Rep. 11 (1) (2021) 10959.
[45] H. Zheng, et al., Metals 11 (2021), doi:10.3390/met11060937.
[46] M. Grasso, et al., Meas. Sci. Technol. 32 (11) (2021) 112001.
[47] A.Y. Al-Maharma, S.P. Patil, B. Markert, Mater. Res. Express 7 (12) (2020) 122001.
[48] A. du Plessis, I. Yadroitsava, I. Yadroitsev, Mater. Des. 187 (2020) 108385.
[49] Z. Snow, et al., Mater. Sci. Eng.: A 864 (2023) 144575.
[50] Q. Luo, et al., Addit. Manuf. 56 (2022) 102915.
[51] X. Gao, et al., Int. J. Fatigue 162 (2022) 106979.
[52] V. Sundar, et al., J. Mater. Eng. Perform. 30 (7) (2021) 4958–4964.
[53] Y. Wang, Z. Su, Theor. Appl. Fract. Mech. 111 (2021) 102849.
[54] V. Manakari, G. Parande, M. Gupta, Metals 7 (2017), doi:10.3390/met7010002.
[55] A.V. Weckman, B.F. Dem'yanov, JETP Lett. 111 (11) (2020) 643–646.